SLAC–PUB–6051
January 1993
(N)

e^+e^- Linear Colliders and New Particle Searches*

TIMOTHY L. BARKLOW

Stanford Linear Accelerator Center
Stanford University, Stanford, California 94309

ABSTRACT

We discuss future e^+e^- linear colliders and new particle searches that can be done with them. In the discussion of new particle searches we examine the following topics: searches for gauge boson structure, searches for a strongly interacting Higgs sector, top quark studies, Higgs searches, supersymmetric particle searches and measurements of soft supersymmetry breaking parameters.

1. Introduction

Physicists from many institutions around the world are currently in the process of defining the physics, machine parameters and machine design of a future e^+e^- linear collider. We will first discuss ideas for future e^+e^- linear collider design and say a few words about the experimental environment at an e^+e^- linear collider. We will begin the discussion of physics topics with the process $e^+e^- \to W^+W^-$. This is an important topic in its own right, but it will also serve to illustrate many of the techniques used in analyzing final states at e^+e^- linear colliders. We will then briefly discuss the physics of top quarks. The remainder of the paper will be devoted to Higgs physics and supersymmetry (SUSY).

Fig. 1 is a schematic of a future e^+e^- linear collider. We shall refer to such a collider as the next linear collider or NLC. All NLC designs share the schematic shown in Fig. 1. Looking at Fig. 1 we see that there are damping rings to reduce the beam emittance, compressors to shorten the length of the e^+e^- bunches, two main accelerators, and two final focus sections.

The initial center-of-mass energy (E_{cm}) of all NLC designs is 500 GeV. Of course the E_{cm} can be lowered to study, for example, the $t\bar{t}$ threshold region. The design luminosity at $E_{cm} = 500$ GeV is about $6 \times 10^{33}\ cm^{-2}s^{-1}$. It will hopefully become clear as we discuss various physics topics why the initial E_{cm} is a good choice and why the luminosity is a good match for this E_{cm}.

The E_{cm} is upgraded by lengthening the accelerator sections, increasing the

*This work supported by the Department of Energy, contract DE–AC03–76SF00515.

Presented at the Trieste Workshop on the Search for New Elementary Particles: Status and Prospects, Trieste, Italy, May 20–22, 1992

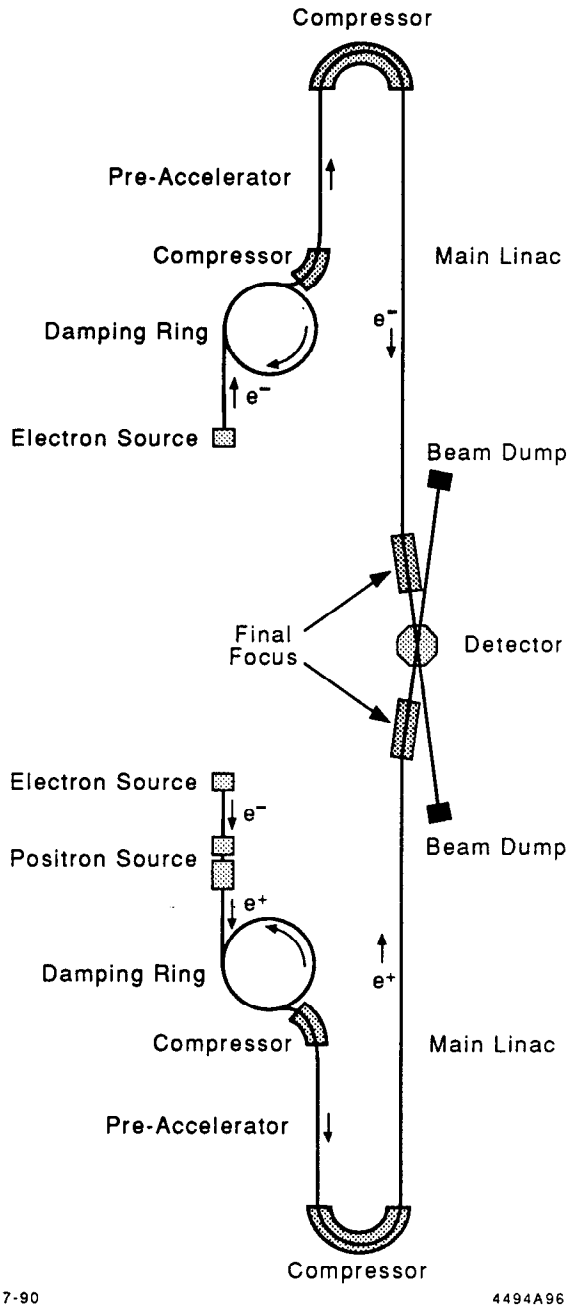

Fig. 1. Schematic diagram of an NLC.

accelerating gradient, or both. The only collider parts which must be moved when lengthening the main accelerators are the bunch compressors at the top and bottom of Fig. 1. These compressors move outward so that the collider is lengthened like a trombone. Most designs envisage an energy upgrade from $E_{cm} = 500$ GeV to $E_{cm} = 1500$ GeV. This factor of 3 increase in NLC energy can be compared to the factor of 2.5 increase in the SLAC energy during its first 20 years of operation,

where the increase at SLAC was accomplished solely by upgrading the accelerating gradient.

Vigorous research and development programs in e^+e^- linear collider design have been under way for many years at SLAC, KEK, DESY and other institutions. With the exception of the main accelerator, there is general agreement on all aspects of NLC design. Three approaches to e^+e^- acceleration have emerged.

SLAC, KEK, and Novosibirsk are proposing[1,2] to extend the Stanford Linear Accelerator technology from the present RF frequency of 3 GHz (S-Band) to an RF frequency of 11.4 GHz (X-Band). When operating at a center-of-mass energy of 500 GeV the X-Band Linac would have an accelerating gradient of 50 MV/m which is to be compared to an accelerating gradient of 17 MV/m for the present S-Band Linac. It is thought that the gradient could be increased to 100 MV/m for operation of the collider at center-of-mass energies of 1.0 to 1.5 TeV The SLAC X-Band design has a repetition rate of 180 Hz with 0.65×10^{10} electrons per bunch and 90 bunches per RF pulse.

A group at DESY is proposing[3] to use the current S-Band technology. The DESY design would therefore have an accelerating gradient of 17 MV/m. The DESY S-Band repetition rate is 50 Hz and there are 0.70×10^{10} electrons per bunch and 172 bunches per RF pulse.

TESLA, a collaboration of physicists from Cornell, CEBAF, DESY, and other institutions, is proposing[4] to use superconducting RF technology. The highest gradient attainable today in a working superconducting RF accelerator is 7 MV/m. The TESLA collabortion believes they can achieve 25 MV/m eventually. The TESLA acclerator would operate at a frequency of 1.5 GHz (L-Band) so that the accelerator structure would be quite large. A larger structure reduces wakefield effects and is therefore an advantage. The TESLA collider has a repetition rate of 10 Hz with 5×10^{10} electrons per bunch and 800 bunches per RF pulse.

The luminosity of all three designs is about $6 \times 10^{33}\ cm^{-2}\ s^{-1}$ at $E_{cm} = 500$ GeV. At 1 TeV the TESLA and X-Band designs have a luminosity of 1 to $2 \times 10^{34}\ cm^{-2}\ s^{-1}$ but the S-Band design is having trouble keeping up at a luminosity of $0.3 \times 10^{34}\ cm^{-2}\ s^{-1}$.

Most of the analyses which we present assume $E_{cm} = 500$ GeV and an integrated luminosity of 10 fb^{-1}. Such an integrated luminosity would correspond to a 10^7 second run at 16% of the design differential luminosity at $E_{cm} = 500$ GeV. We note that the SLAC linear collider (SLC), an add–on to a 30 year old accelerator, currently operates at 15% of its design luminosity.

We will not talk about detectors at future e^+e^- linear colliders. For most physics analyses the features and resolution of existing e^+e^- collider detectors, such as SLD and the LEP detectors, are sufficient. Indeed, the resolution of SLD/LEP

detectors is assumed for all the analyses described in this article. That is not to say that these detectors can be transplanted without modification to the interaction point of an NLC. There are new sources of backgrounds at an NLC, such as muons created upstream of the interaction point, and a large number of e^+e^- pairs produced each bunch crossing due to the large luminosity per bunch crossing. However, even with these and other constraints on detector design, it is felt that all of the features of SLD/LEP detectors can be retained and that the existing resolution specifications can be met or exceeded[5]

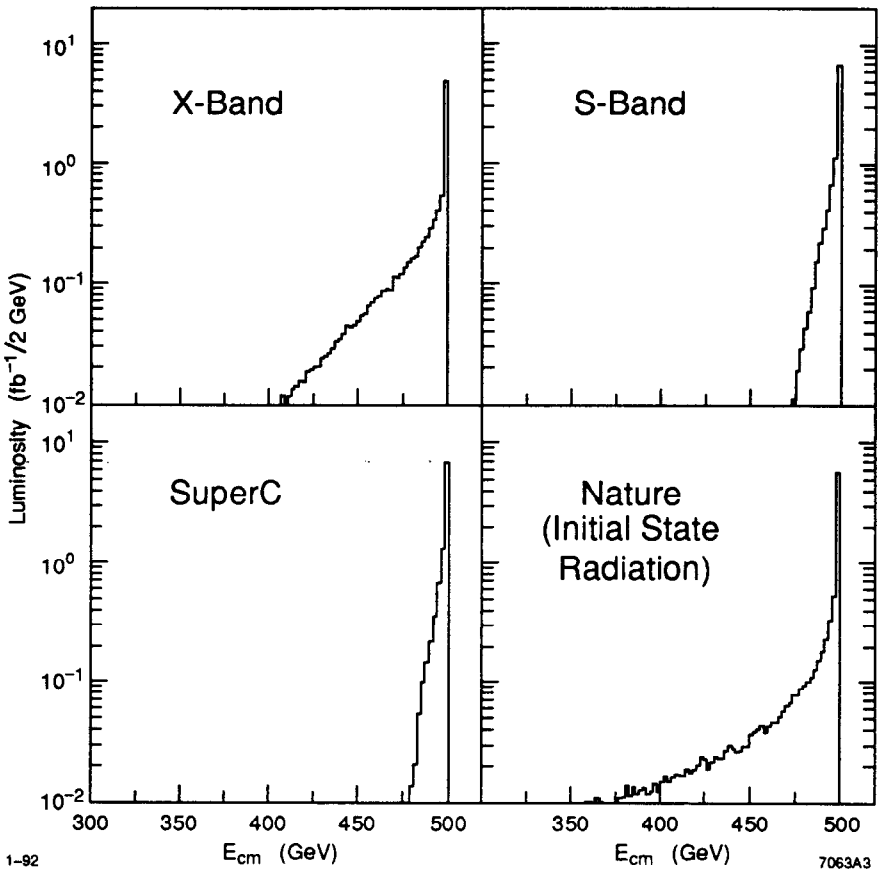

Fig. 2. e^+e^- luminosity spectra.

One important difference between the experimental environments at e^+e^- storage rings and future e^+e^- linear colliders is the presence of beamstrahlung at linear colliders. Beamstrahlung is the radiation by particles of one bunch as they bend in the intense collective magnetic field of the opposing bunch. Fig. 2 shows the one-dimensional luminosity-weighted e^+e^- E_{cm} distributions[6] for the three types of

accelerators. The extent to which each distribution deviates from a delta function reflects the amount of beamstrahlung radiation emitted during a bunch crossing. Also shown is the e^+e^- E_{cm} distribution for a machine without beamstrahlung but with the effects of initial state radiation included. We see that the magnitude of the beamstrahlung radiation is equal to or less than the bremsstrahlung radiation we are accustomed to. Beamstrahlung radiation modifies the irreducible bremsstrahlung radiation spectrum but does not introduce anything new.

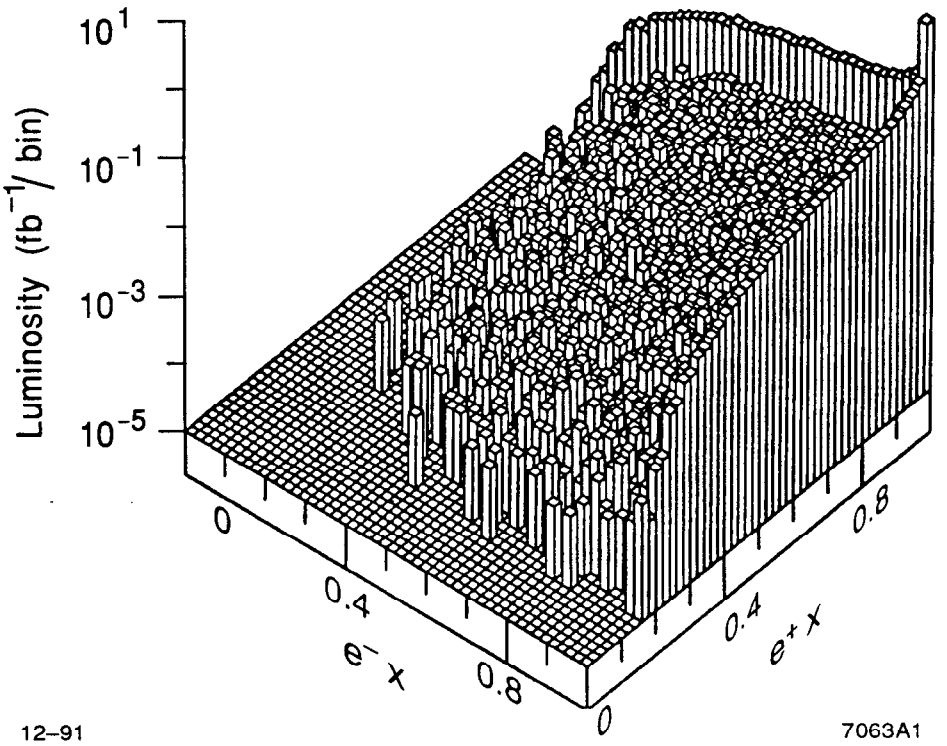

Fig. 3. e^+e^- luminosity spectrum as a function of the fractional electron energy (e^- x) and the fractional positron energy (e^+ x), for a machine design with an exceptionally large amount of beamstrahlung radiation (no design currently being considered has this much radiation). Loss from beamstrahlung radiation only is included.

In Fig. 3 we show the two-dimensional luminosity-weighted e^+e^- fractional energy distribution with beamstrahlung included but bremsstrahlung excluded. Note that the vertical scale is logarithmic. The highest bin is for the case where neither e^+ or e^- radiates a beamstrahlung photon. The second most likely case is that one, but not both, of the e^+ and e^- radiate a photon. The least likely case is when both the e^+ and e^- radiate a beamstrahlung photon. This means, for example, that it is a pretty good approximation to assume that neither the e^+

or e^- has radiated when performing beam energy–momemtum constraints on the final state momenta, that it is a better approximation to assume that only one of the e^+e^- has radiated, and that it is only necessary for very high precision analyses to allow for radiation by both the e^+ and e^-.

2. Gauge Boson Compositeness

Remarkably little is known about the interactions of the electroweak gauge bosons with each other. There are two distinct aspects of these interactions which are of interest. First, the triple and quartic gauge boson vertices need to be tested for any structure beyond what is produced by Standard Model radiative corrections. Such anomalous structure would appear, for example, if the W and Z bosons were themselves composite objects. Second, gauge boson scattering processes such as $W^+W^- \to W^+W^-$ can help us understand the mechanism responsible for electroweak symmetry breaking. W^+W^- scattering processes can be studied at an e^+e^- collider either by radiating virtual W's off of the e^- and e^+, or by studying W^+W^- rescattering in $e^+e^- \to W^+W^-$.

2.1 *Parameterization of Three Gauge Boson Vertex*

We use the formalism of Ref. 7 to describe the general W^+W^-V vertex, where $V = \gamma, Z$. The effective Lagrangian for the general W^+W^-V vertex as given in Eq.(2.1) of Ref. 7 is:

$$\begin{aligned}\mathcal{L}_{WWV}/g_{WWV} = {} & ig_1^V(W^\dagger_{\mu\nu}W^\mu V^\nu - W^\dagger_\mu V_\nu W^{\mu\nu}) + i\kappa_V W^\dagger_\mu W_\nu V^{\mu\nu} \\ & + \frac{i\lambda_V}{m_W^2} W^\dagger_{\lambda\mu} W^\mu{}_\nu V^{\nu\lambda} - g_4^V W^\dagger_\mu W_\nu(\partial^\mu V^\nu + \partial^\nu V^\mu) \\ & + g_5^V \varepsilon^{\mu\nu\rho\sigma}(W^\dagger_\mu \overleftrightarrow{\partial}_\rho W_\nu)V_\sigma + i\tilde{\kappa_V} W^\dagger_\mu W_\nu \tilde{V}^{\mu\nu} \\ & + \frac{i\tilde{\lambda}_V}{m_W^2} W^\dagger_{\lambda\mu} W^\mu{}_\nu \tilde{V}^{\nu\lambda} \quad .\end{aligned} \tag{1}$$

The terms with the coupling parameters g_1^V, κ_V, λ_V separately conserve C, P, and T, while the others violate C or P, or both. We will concentrate in this article on measurements of the coupling parameters κ_γ, λ_γ, κ_Z, and λ_Z.

In the standard model, at tree-level, $g_1^\gamma = g_1^Z = 1$, $\kappa_\gamma = \kappa_Z = 1$ and all other coupling parameters in Eq. (1) are 0. There is currently much discussion in the literature[8,9] regarding the extent to which present day electroweak measurements, especially precision LEP measurements, constrain κ_V and λ_V. In order to set the

stage for our discussion of the limits obtainable with the NLC, we quote the results of Kane *et al.*[8] who considered loop effects and unitarity constraints:

$$|\lambda_\gamma| \leq 0.6 \quad |\kappa_\gamma - 1| \leq 1.0$$
$$|\lambda_Z| \leq 0.6 \quad -0.8 \leq \kappa_Z - 1 \leq 0.0$$

where $\kappa_V - 1 \equiv \kappa_V - 1$. These authors also estimated that the SSC should achieve limits on λ_γ and κ_γ of

$$|\lambda_\gamma| \leq 0.02 \quad |\kappa_\gamma - 1| \leq 0.1$$

with 10 fb^{-1}.

2.2 *Final State Helicity Analysis of* $e^+e^- \rightarrow W^+W^-$

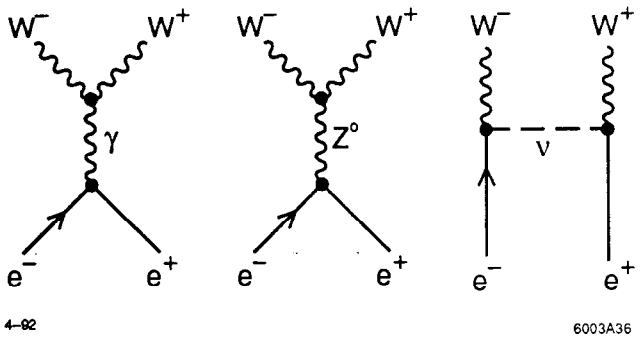

Fig. 4. The three tree-level Feynman diagrams for the process $e^+e^- \rightarrow W^+W^-$.

We start our discussion of $e^+e^- \rightarrow W^+W^-$ with some definitions. Following Ref. 7 we define our z-axis to be the direction of the W^- in the e^+e^- rest frame. The W^- production angle Θ is defined to be the angle between the initial state e^- and the W^- in the e^+e^- rest frame. The W^- and W^+ decay according to $W^- \rightarrow f_1\overline{f}_2$ and $W^+ \rightarrow f_3\overline{f}_4$. We define θ and ϕ to be the polar and azimuthal angles, respectively, of the fermion f_1 in the W^- rest frame, while $\overline{\theta}$ and $\overline{\phi}$ are the polar and azimuthal angles, respectively, of the anti-fermion $\overline{f}_4$ in the W^+ rest frame. We assume that the e^- beam has the polarization P_e where $P_e = 1$ is 100% right-handed and $P_e = -1$ is 100% left-handed.

$e^+e^- \rightarrow W^+W^-$ proceeds through the three Feynman diagrams shown in Fig. 4. The differential cross-section $d\sigma/\cos\Theta$ is shown in Fig. 5, with the cross-section decomposed into different W^+W^- helicity combinations. Our notation is such that $(\lambda,\overline{\lambda})$ indicates that the W^- has helicity λ, the W^+ has helicity $\overline{\lambda}$,

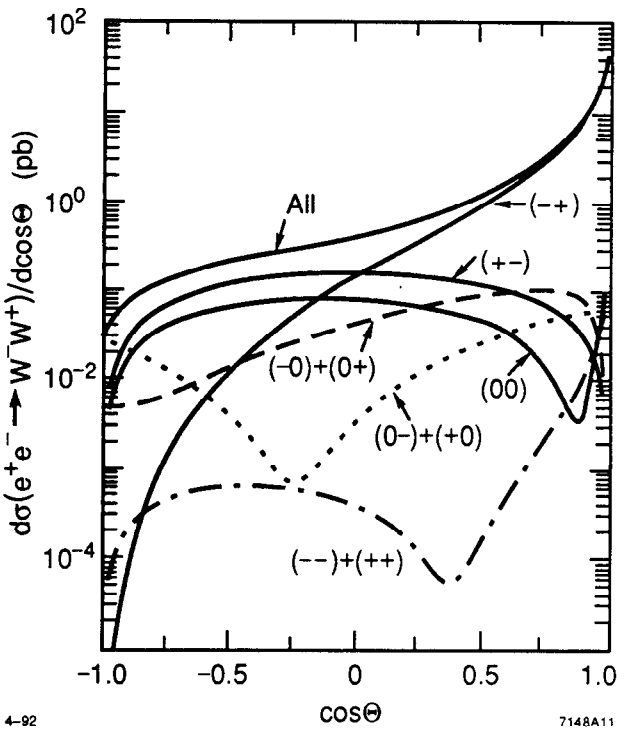

Fig. 5. The differential cross-section $d\sigma/\cos\Theta$ for $e^+e^- \rightarrow W^+W^-$ with the cross-section decomposed into different W^+W^- helicity combinations.

and that $\lambda = +, -, 0$ refers to right-handed transverse, left-handed transverse, and logitudinal W's, respectively. At forward angles the t-channel neutrino exchange diagram dominates and the cross-section consists almost entirely of left-handed transverse W^- and right-handed transverse W^+ gauge bosons. Transverse W's continue to dominate the cross-section at central angles. Only when $\cos\Theta$ drops below -0.9 do helicity combinations with at least one longitudinal gauge boson become important. The production angle θ therefore provides only limited information about individual W^+W^- helicity combinations.

The decay angles θ and ϕ can be used to improve the W^+W^- helicity analysis. To understand in detail how the decay angles reflect the helicity of the parent W we must look at the multi-differential cross-section for W^+W^- production and decay. The expression for the multi-differential cross-section depends on the event topology we are analyzing. Throughout this chapter we will concentrate on events where one W decays leptonically and the other decays hadronically. This topology has good statistics, can be separated from background with a high degree of purity, is rich in helicity information, and allows us to reconstruct all final state variables on an event-by-event basis. For events where the W^- decays leptonically and the W^+ decays hadronically (*topology A* events) the multi-differential cross section is

given by:

$$\frac{\mathrm{d}\sigma(\kappa_\gamma,\lambda_\gamma,\kappa_Z,\lambda_Z;\cos\Theta,\cos\theta,\phi,\cos\overline{\theta},\overline{\phi},P_e)}{\mathrm{d}\cos\Theta\ \mathrm{d}\cos\theta\ \mathrm{d}\phi\ \mathrm{d}\cos\overline{\theta}\ \mathrm{d}\overline{\phi}} =$$

$$\frac{9\beta B_{lh}}{8192\pi^3 s}\sum_{\lambda,\lambda',\overline{\lambda},\overline{\lambda}'}\mathcal{Q}^{\lambda\overline{\lambda}}_{\lambda'\overline{\lambda}'}(\kappa_\gamma,\lambda_\gamma,\kappa_Z,\lambda_Z;\cos\Theta,P_e)\mathcal{D}^{\lambda}_{\lambda'}(\cos\theta,\phi)\overline{\mathcal{H}}^{\overline{\lambda}}_{\overline{\lambda}'}(\cos\overline{\theta},\overline{\phi}) \qquad (2)$$

where

$$\begin{aligned}\mathcal{Q}^{\lambda\overline{\lambda}}_{\lambda'\overline{\lambda}'} \equiv &(1+P_e)\sum_{\overline{\sigma}}\mathcal{M}_1(+,\overline{\sigma},\lambda,\overline{\lambda};\Theta)\mathcal{M}_1^*(+,\overline{\sigma},\lambda',\overline{\lambda}';\Theta)\\ &+(1-P_e)\sum_{\overline{\sigma}}\mathcal{M}_1(-,\overline{\sigma},\lambda,\overline{\lambda};\Theta)\mathcal{M}_1^*(-,\overline{\sigma},\lambda',\overline{\lambda}';\Theta)\quad .\end{aligned}$$

and

$$\overline{\mathcal{H}}^{\overline{\lambda}}_{\overline{\lambda}'}(\cos\overline{\theta},\overline{\phi}) \equiv \left[\overline{\mathcal{D}}^{\overline{\lambda}}_{\overline{\lambda}'}(\cos\overline{\theta},\overline{\phi}) + \overline{\mathcal{D}}^{\overline{\lambda}}_{\overline{\lambda}'}(-\cos\overline{\theta},\overline{\phi}+\pi)\right] \quad .$$

The W^+W^- production amplitude $\mathcal{M}_1$, the W^- decay tensor $\mathcal{D}^{\lambda}_{\lambda'}$ and the W^+ decay tensor $\overline{\mathcal{D}}^{\overline{\lambda}}_{\overline{\lambda}'}$ are defined in Ref. 7. We note that

$$\mathcal{P}^{\lambda\overline{\lambda}}_{\lambda'\overline{\lambda}'} = \mathcal{Q}^{\lambda\overline{\lambda}}_{\lambda'\overline{\lambda}'}\,|_{P_e=0}$$

where $\mathcal{P}^{\lambda\overline{\lambda}}_{\lambda'\overline{\lambda}'}$ is the W^+W^- production tensor defined in Eq. 4.11 of Ref. 7. In Eq. (2), $\sqrt{s}$ is the e^+e^- center-of-mass energy, $\beta = \sqrt{1-4m_W^2/s}$ and B_{lh} is the product of the leptonic and hadronic branching ratios for the W boson. The sum $\overline{\mathcal{H}}^{\overline{\lambda}}_{\overline{\lambda}'}(\cos\overline{\theta},\overline{\phi})$ appears in Eq. (2), instead of the single term $\overline{\mathcal{D}}^{\overline{\lambda}}_{\overline{\lambda}'}(\cos\overline{\theta},\overline{\phi})$, because we assume that we cannot tag the flavor of the the quark jets in the decay of the W^+. When the W^+ decays leptonically and the W^- decays hadronically (*topology B*) we use the cross-section

$$\frac{\mathrm{d}\overline{\sigma}(\kappa_\gamma,\lambda_\gamma,\kappa_Z,\lambda_Z;\cos\Theta,\cos\overline{\theta},\overline{\phi},\cos\theta,\phi,P_e)}{\mathrm{d}\cos\Theta\ \mathrm{d}\cos\theta\ \mathrm{d}\phi\ \mathrm{d}\cos\overline{\theta}\ \mathrm{d}\overline{\phi}} =$$

$$\frac{9\beta B_{lh}}{8192\pi^3 \mathrm{s}}\sum_{\lambda,\lambda',\overline{\lambda},\overline{\lambda}'}\mathcal{Q}^{\lambda\overline{\lambda}}_{\lambda'\overline{\lambda}'}(\kappa_\gamma,\lambda_\gamma,\kappa_Z,\lambda_Z;\cos\Theta,P_e)\mathcal{H}^{\lambda}_{\lambda'}(\cos\overline{\theta},\overline{\phi})\overline{\mathcal{D}}^{\overline{\lambda}}_{\overline{\lambda}'}(\cos\overline{\theta},\overline{\phi}) \qquad (3)$$

where

$$\mathcal{H}^{\lambda}_{\lambda'}(\cos\overline{\theta},\overline{\phi}) \equiv \left[\mathcal{D}^{\lambda}_{\lambda'}(\cos\theta,\phi) + \mathcal{D}^{\lambda}_{\lambda'}(-\cos\theta,\phi+\pi)\right] \quad .$$

The W^- decay tensor $\mathcal{D}^{\lambda}_{\lambda'}(\cos\theta,\phi)$ is given explicitly by

$$\begin{aligned}
\mathcal{D}^{+}_{+} &= \frac{1}{2}(1-\cos\theta)^2, \qquad \mathcal{D}^{-}_{-} = \frac{1}{2}(1+\cos\theta)^2, \qquad \mathcal{D}^{0}_{0} = \sin^2\theta, \\
\mathcal{D}^{+}_{0} &= \frac{1}{\sqrt{2}}(1-\cos\theta)\sin\theta e^{i\phi}, \\
\mathcal{D}^{-}_{0} &= -\frac{1}{\sqrt{2}}(1+\cos\theta)\sin\theta e^{-i\phi}, \\
\mathcal{D}^{+}_{-} &= \frac{1}{2}\sin^2\theta e^{2i\phi},
\end{aligned} \tag{4}$$

and $\mathcal{D}^{\lambda'}_{\lambda} = (\mathcal{D}^{\lambda}_{\lambda'})^*$. We also show explicitly the expression for the W^- hadronic decay tensor $\mathcal{H}^{\lambda}_{\lambda'}(\cos\theta,\phi)$:

$$\begin{aligned}
\mathcal{H}^{+}_{+} &= 1+\cos^2\theta, \qquad \mathcal{H}^{-}_{-} = 1+\cos^2\theta, \qquad \mathcal{H}^{0}_{0} = 2\sin^2\theta, \\
\mathcal{H}^{+}_{0} &= \sqrt{2}\cos\theta\sin\theta e^{i\phi} \\
\mathcal{H}^{-}_{0} &= -\sqrt{2}\cos\theta\sin\theta e^{-i\phi} \\
\mathcal{H}^{+}_{-} &= \sin^2\theta e^{2i\phi}
\end{aligned} \tag{5}$$

Although the W^- hadronic decay tensor $\mathcal{H}^{\lambda}_{\lambda'}(\cos\theta,\phi)$ does not contain as much helicity information as the leptonic decay tensor $\mathcal{D}^{\lambda}_{\lambda'}(\cos\theta,\phi)$, its information content is nevertheless non-negligible.

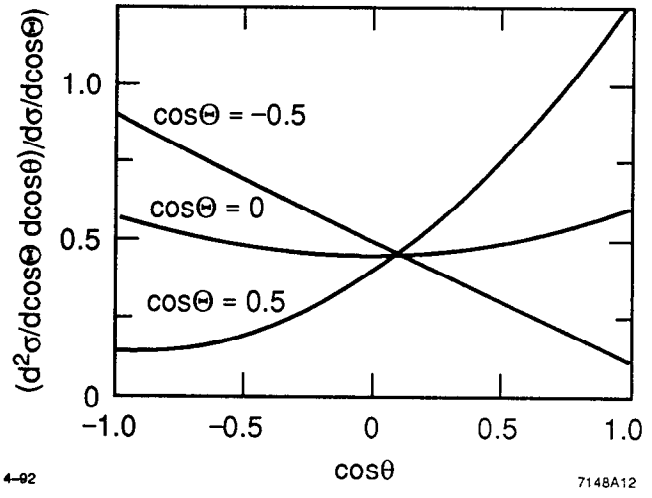

Fig. 6. Distributions in $d\sigma/\cos\theta$ for various values of $\cos\Theta$.

The decay tensor components $\mathcal{D}^{+}_{+}$, $\mathcal{D}^{-}_{-}$, and $\mathcal{D}^{0}_{0}$ for pure left-handed transverse, pure right-handed transverse, and pure longitudinal W^- gauge bosons, respectively, have distinctive polar angle distributions, and do not exhibit an azimuthal

angle dependence. Distributions in $\mathrm{d}\sigma/\cos\theta$ are shown in Fig. 6 for various values of $\cos\Theta$. At $\cos\Theta = +0.5$ we can see from the $\cos\theta$ distribution that the W^- is almost entirely left-handed. On the other hand, at $\cos\Theta = 0$ and $\cos\Theta = -0.5$ the W^- is a mixture of various polarizations.

The interference terms in Eq. (4) do depend on the decay azimuthal angle. For example, the decay tensor component $\mathcal{D}_0^0$ for the pure longitudinal W^- boson is indistinguishable from the component $\mathcal{D}_-^+$ for the interference between left-handed and right-handed transverse W^- bosons, except for the azimuthal angle factor $\mathrm{e}^{2i\phi}$. Our set of experimental observables therefore includes not only the cosines of the polar angles, $\cos\Theta$, $\cos\theta$, and $\cos\overline{\theta}$, but also the azimuthal angles ϕ and $\overline{\phi}$. Our full helicity analysis then consists of a maximum likelihood fit of the form

$$\ln L(\kappa_\gamma, \lambda_\gamma, \kappa_Z, \lambda_Z; \mathcal{L}_k) = \sum_{i_1=1}^{N_\Theta}\sum_{i_2=1}^{N_\theta}\sum_{i_3=1}^{N_\phi}\sum_{i_4=1}^{N_{\overline{\theta}}}\sum_{i_5=1}^{N_{\overline{\phi}}}\sum_{k=1}^{N_{P_e}} \Big[r_{i_1 i_2 i_3 i_4 i_5 k} \ln(\mu_{i_1 i_2 i_3 i_4 i_5 k}) - \mu_{i_1 i_2 i_3 i_4 i_5 k} + \overline{r}_{i_1 i_2 i_3 i_4 i_5 k} \ln(\overline{\mu}_{i_1 i_2 i_3 i_4 i_5 k}) - \overline{\mu}_{i_1 i_2 i_3 i_4 i_5 k} \Big] \quad (6)$$

where $r_{i_1 i_2 i_3 i_4 i_5 k}$ and $\mu_{i_1 i_2 i_3 i_4 i_5 k}$ are the measured number of topology A events and the expected number of topology A events, respectively, in the bin centered at $\cos\Theta_{i_1}$, $\cos\theta_{i_2}$, ϕ_{i_3}, $\cos\overline{\theta}_{i_4}$, $\overline{\phi}_{i_5}$, when the e^- polarization is P_{ek}. $\overline{r}_{i_1 i_2 i_3 i_4 i_5 k}$ and $\overline{\mu}_{i_1 i_2 i_3 i_4 i_5 k}$ are the measured and expected number of topology B events. The volume of a bin is

$$\Delta\Omega = \frac{16\pi^2}{N_\Theta N_\theta N_\phi N_{\overline{\theta}} N_{\overline{\phi}}} \quad .$$

We define $\mu_{i_1 i_2 i_3 i_4 i_5 k}$ as follows:

$$\mu_{i_1 i_2 i_3 i_4 i_5 k}(\kappa_\gamma, \lambda_\gamma, \kappa_Z, \lambda_Z, \mathcal{L}_k) \equiv \mathcal{L}_k \int_{\eta_{i_1}^-}^{\eta_{i_1}^+} \mathrm{d}\cos\Theta \int_{\eta_{i_2}^-}^{\eta_{i_2}^+} \mathrm{d}\cos\theta \int_{\eta_{i_3}^-}^{\eta_{i_3}^+} \mathrm{d}\phi \int_{\eta_{i_4}^-}^{\eta_{i_4}^+} \mathrm{d}\cos\overline{\theta} \int_{\eta_{i_5}^-}^{\eta_{i_5}^+} \mathrm{d}\overline{\phi}$$

$$\left\{ \frac{\mathrm{d}\xi(\cos\Theta, \cos\theta, \phi, \cos\overline{\theta}, \overline{\phi}, P_{ek})}{\mathrm{d}\cos\Theta\ \mathrm{d}\cos\theta\ \mathrm{d}\phi\ \mathrm{d}\cos\overline{\theta}\ \mathrm{d}\overline{\phi}} + \left[\int_{-1}^{1} \mathrm{d}\cos\Theta' \int_{-1}^{1} \mathrm{d}\cos\theta' \int_{0}^{2\pi} \mathrm{d}\phi' \int_{0}^{1} \mathrm{d}\cos\overline{\theta}' \int_{0}^{2\pi} \mathrm{d}\overline{\phi}' \right.\right.$$

$$G(\cos\Theta, \cos\theta, \phi, \cos\overline{\theta}, \overline{\phi}; \cos\Theta', \cos\theta', \phi', \cos\overline{\theta}', \overline{\phi}')$$

$$\left.\left. \cdot \frac{\mathrm{d}\sigma(\kappa_\gamma, \lambda_\gamma, \kappa_Z, \lambda_Z; \cos\Theta', \cos\theta', \phi', \cos\overline{\theta}', \overline{\phi}', P_{ek})}{\mathrm{d}\cos\Theta'\ \mathrm{d}\cos\theta'\ \mathrm{d}\phi'\ \mathrm{d}\cos\overline{\theta}'\ \mathrm{d}\overline{\phi}'} \right] \right\}$$

where

$$\eta_{i_1}^{\pm} = \cos\Theta_{i_1} \pm \frac{1}{N_\Theta}; \qquad \eta_{i_2}^{\pm} = \cos\theta_{i_2} \pm \frac{1}{N_\theta}; \qquad \eta_{i_3}^{\pm} = \phi_{i_3} \pm \frac{\pi}{N_\phi}$$

$$\eta_{i_4}^{\pm} = \cos\overline{\theta}_{i_4} \pm \frac{1}{2N_{\overline{\theta}}}; \qquad \eta_{i_5}^{\pm} = \overline{\phi}_{i_5} \pm \frac{\pi}{N_{\overline{\phi}}}$$

and

$$\frac{\mathrm{d}\xi(\cos\Theta, \cos\theta, \phi, \cos\overline{\theta}, \overline{\phi}, P_e)}{\mathrm{d}\cos\Theta\ \mathrm{d}\cos\theta\ \mathrm{d}\phi\ \mathrm{d}\cos\overline{\theta}\ \mathrm{d}\overline{\phi}}$$

is the multi-differential cross-section for background processes that pass all the W^+W^- analysis cuts. The function

$$G(\cos\Theta, \cos\theta, \phi, \cos\overline{\theta}, \overline{\phi}; \cos\Theta', \cos\theta', \phi', \cos\overline{\theta}', \overline{\phi}')$$

is the resolution function for our $e^+e^- \to W^+W^-$ analysis. It is defined so that $G\mathrm{d}\Omega$ is the probability that a W^+W^- pair produced with the variables

$$\cos\Theta', \cos\theta', \phi', \cos\overline{\theta}', \text{ and } \overline{\phi}'$$

passes all the W^+W^- analysis cuts and is placed in a bin of volume $\mathrm{d}\Omega$ centered at

$$\cos\Theta, \cos\theta, \phi, \cos\overline{\theta}, \overline{\phi}\ .$$

We shall assume that the W^+W^- final state can be isolated sufficiently well that

$$\frac{\mathrm{d}\xi(\cos\Theta, \cos\theta, \phi, \cos\overline{\theta}, \overline{\phi}, P_e)}{\mathrm{d}\cos\Theta\ \mathrm{d}\cos\theta\ \mathrm{d}\phi\ \mathrm{d}\cos\overline{\theta}\ \mathrm{d}\overline{\phi}} = 0,$$

is a good approximation. Although we are confident that this indeed is a good approximation, it remains an important topic of future study to actually prove that this will be the case.

For most of the results that are presented in this chapter we assume that there is no initial state radiation, beamstrahlung or intrinsic linac energy spread. Furthermore, we assume that we have a perfect detector that can measure the variables $\cos\Theta, \cos\theta, \phi, \cos\overline{\theta}, \overline{\phi}$ with 100% efficiency and infinite accuracy for topology A and B events with $|\cos\Theta| < 0.8$:

$$G(\Omega;\Omega') = \begin{cases} \delta^5(\Omega;\Omega'), & \text{if } |\cos\Theta| < 0.8; \\ 0, & \text{otherwise,} \end{cases}$$

where we have used Ω to denote the set of variabes $\cos\Theta$, $\cos\theta$, ϕ, $\cos\overline{\theta}$, and $\overline{\phi}$. We shall also assume for most of this chapter that $G(\Omega;\Omega') = 0$ for topology A

and B events in which the W decays via $W \rightarrow \tau\nu$. The only source of error remaining after we make these assumptions is the statistical error associated with each bin count. At the end of the chapter we shall discuss how initial state radiation and beamstrahlung might be dealt with, and we investigate how our results are changed once detector resolution and $W \rightarrow \tau\nu$ decays are incorporated into a realistic resolution function.

We first fix κ_Z and λ_Z at their standard model values and do a three parameter log-likelihood fit of κ_γ, λ_γ, and $\mathcal{L}$. Here, and throughout this chapter, we use a binning of

$$N_\Theta = 20 \quad \text{and} \quad N_\theta = N_\phi = N_{\bar{\theta}} = N_{\bar{\phi}} = 5 \ .$$

This choice was driven by computer CPU and memory considerations. We don't know if a a finer binning granularity can improve our results. Fig. 7 shows 95% confidence level contours for three different center-of-mass energies. The luminosities of 1.3 fb^{-1} at $\sqrt{s} = 200$ GeV, 10 fb^{-1} at $\sqrt{s} = 500$ GeV, and 44 fb^{-1} at $\sqrt{s} = 1000$ GeV were chosen to give roughly 4100 detected events at each of the three center-of-mass energies. Fig. 7(a) shows the 95% confidence level contours for $\sqrt{s} = 200$ GeV and $\sqrt{s} = 500$ GeV; the contour for $\sqrt{s} = 1000$ GeV is too small to appear on this scale. Also shown in Fig. 7(a) is an estimate[8] of the 95% confidence level contour for the SSC at 10 fb^{-1}. There is a significant improvement in the limits in going from $\sqrt{s} = 200$ GeV to $\sqrt{s} = 500$ GeV. Note that the 95% confidence limits from a $\sqrt{s} = 500$ GeV e^+e^- collider at 10 fb^{-1} are much better than the limits estimated in Ref. 8 for the SSC at 10 fb^{-1}. Fig. 7(b) shows the 95% confidence level contour for $\sqrt{s} = 500$ GeV in more detail, and it also shows the contour for $\sqrt{s} = 1000$ GeV. We can see that the individual bounds on κ_γ and λ_γ at $\sqrt{s} = 500$ GeV are $|\kappa_\gamma - 1|, \lambda_\gamma < 0.01$.

Next, we allow all four of our couplings parameters to be free as we perform a six parameter maximum log-likelihood fit of $\kappa_\gamma, \lambda_\gamma, \kappa_Z, \lambda_Z, \mathcal{L}_+, \mathcal{L}_-$. The symbols $\mathcal{L}_+$ and $\mathcal{L}_-$ refer to the luminosities of two runs at different e^- polarizations. We will first assume that $P_e = 0$ for both of these runs and that $\mathcal{L}_+ = \mathcal{L}_- = 5\ fb^{-1}$. The projection onto the $(\kappa_\gamma, \lambda_\gamma)$ and (κ_Z, λ_Z) planes of the six-dimensional 95% confidence level joint probability ellipsoid is shown in Fig. 8. The two-dimensional projection of the six-dimensional ellipsoid is not a nice contour, presumably because the shape of the six-dimensional object is so complicated. Each point is generated by first choosing a direction at random in the six-dimensional space, then traveling in this direction from the standard model point to the surface of the 95% confidence level ellipsoid, and finally projecting this point onto the plane. We interpret the outer boundary of the set of points in Fig. 8(a) to be the 95% confidence level contour for κ_γ and λ_γ, independent of κ_Z and λ_Z. If we compare Figs. 7(b) and 8(a) we see that our individual bounds on κ_γ and λ_γ are degraded by a factor of about

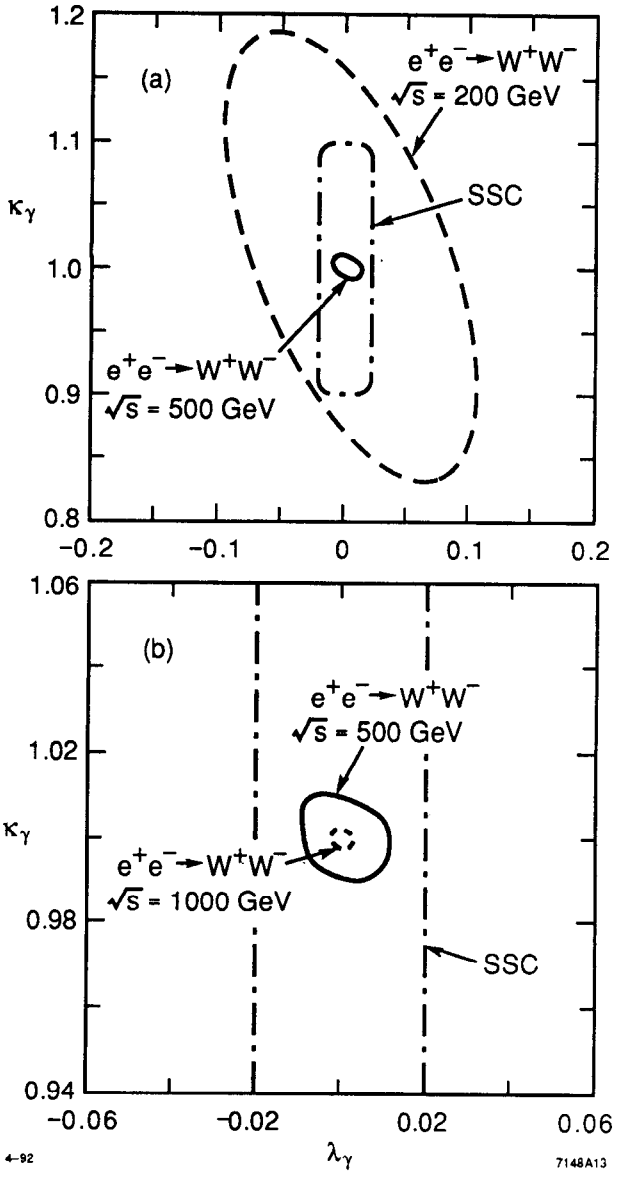

Fig. 7. Projection onto the $(\kappa_\gamma, \lambda_\gamma)$ plane of the 95% confidence level joint probability ellipsoid for a three-parameter maximum likelihood fit of $\kappa_\gamma, \lambda_\gamma, \mathcal{L}$. Standard model values are assumed for κ_Z and λ_Z. Projections for e^+e^- colliders with 1.3 fb^{-1} at $\sqrt{s}$ = 200 GeV, 10 fb^{-1} at $\sqrt{s}$ = 500 GeV, and 44 fb^{-1} at $\sqrt{s}$ = 1000 GeV are plotted, as well as an estimate of the limits from the SSC with 10 fb^{-1} (the SSC limit is independent of κ_Z and lz).

five when we allow all four of our coupling parameters to vary. The individual bounds on κ_γ and λ_γ are now $|\kappa_\gamma - 1|, \lambda_\gamma < 0.05$. Comparing Figs. 8(a) and (b) we see that the area of the excluded region in (κ_Z, lz) space is roughly the same as the excluded area in $(\kappa_\gamma, \lambda_\gamma)$ space.

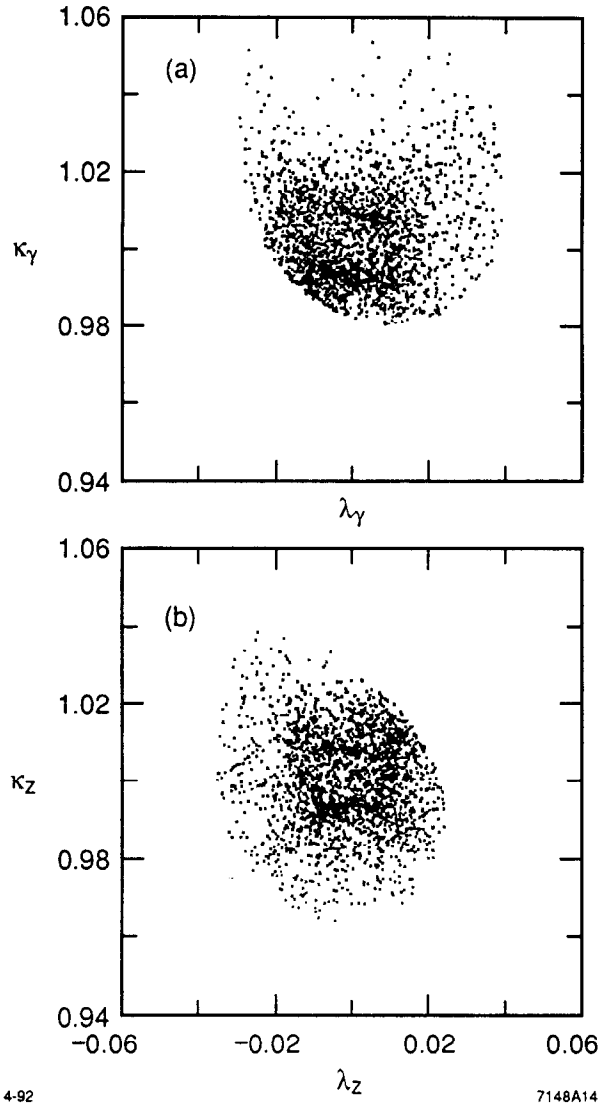

Fig. 8. Projection onto the (a) $(\kappa_\gamma, \lambda_\gamma)$ plane and (b) (κ_Z, λ_Z) plane of the 95% confidence level joint probability ellipsoid for a six parameter maximum likelihood fit of $\kappa_\gamma, \lambda_\gamma, \kappa_Z, \lambda_Z, \mathcal{L}_+, \mathcal{L}_-$. Unpolarized beams are assumed with $\mathcal{L}_+ + \mathcal{L}_- = 10\ fb^{-1}$ at $\sqrt{s} = 500$ GeV.

Given that the e^+e^-Z vertex is parity violating while the $e^+e^-\gamma$ vertex is parity conserving, it might seem plausible that polarized electron beams could help separate anomalous κ_γ and λ_γ values from anomalous κ_Z and λ_Z values. This indeed is the case. In Fig. 9 we show the projections of the six-dimensional 95% confidence level joint probability ellipsoid assuming that $\mathcal{L}_+ = 5\ fb^{-1}$ is collected with 90% right-handed electrons and $\mathcal{L}_- = 5\ fb^{-1}$ is collected with 90% left-handed electrons, all at $\sqrt{s} = 500$ GeV. $\kappa_\gamma - 1$ and λ_γ are now each bounded by ± 0.02 .

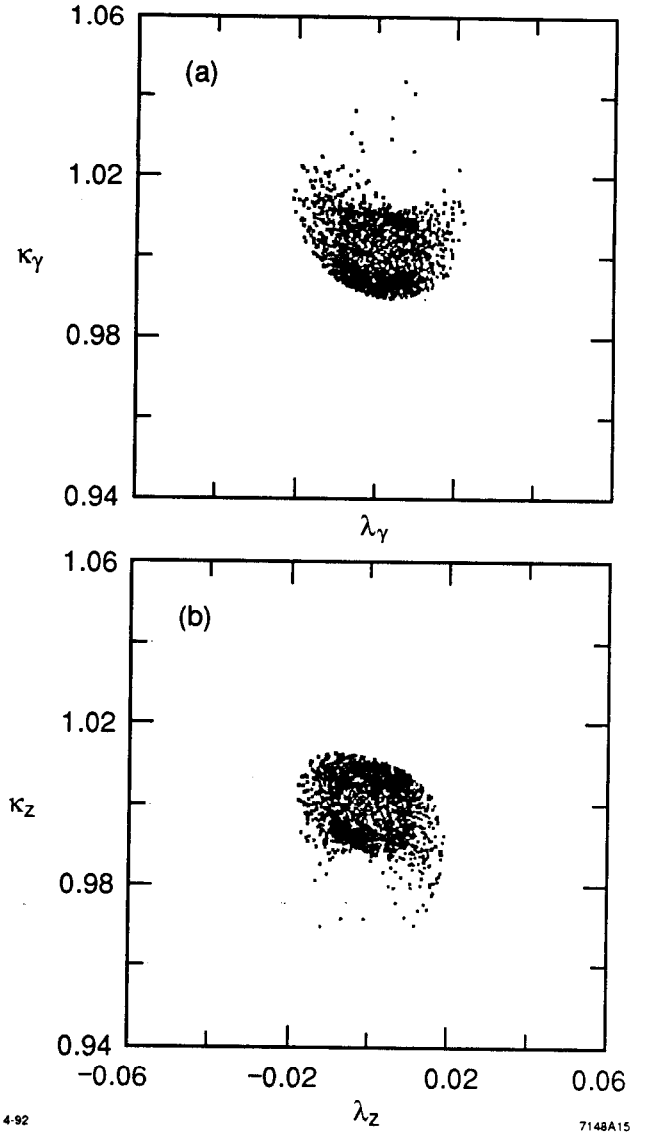

Fig. 9. Projection onto the (a) $(\kappa_\gamma, \lambda_\gamma)$ plane and (b) (κ_Z, λ_Z) plane of the 95% confidence level joint probability ellipsoid for a six-parameter maximum likelihood fit of $\kappa_\gamma, \lambda_\gamma, \kappa_Z, \lambda_Z, \mathcal{L}_+, \mathcal{L}_-$. The data set consisted of $\mathcal{L}_+ = 5\ fb^{-1}$ of 90% right-handed electrons and $\mathcal{L}_- = 5\ fb^{-1}$ of 90% left-handed electrons at $\sqrt{s} = 500$ GeV.

2.3 *A Strongly Interacting Higgs Sector*

Final state rescattering in $e^+e^- \to W^+W^-$, shown diagramatically in Fig. 10, can give us information about the $J = 1$ partial wave in the scattering process $W_L^+W_L^- \to W_L^+W_L^-$, where W_L^- denotes a longitudinally polarized W^- boson. This is discussed, for example, in Refs. 10 and 11. The effect of a 1.8 TeV techni-ρ resonance in the $W_L^+W_L^- \to W_L^+W_L^-$ channel on the $e^+e^- \to W^+W^-$ cross-section

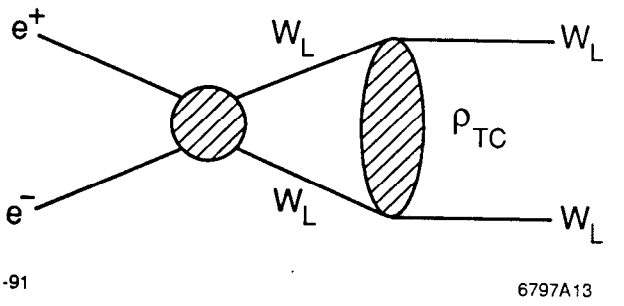

Fig. 10. Final state rescattering in $e^+e^- \to W^+W^-$

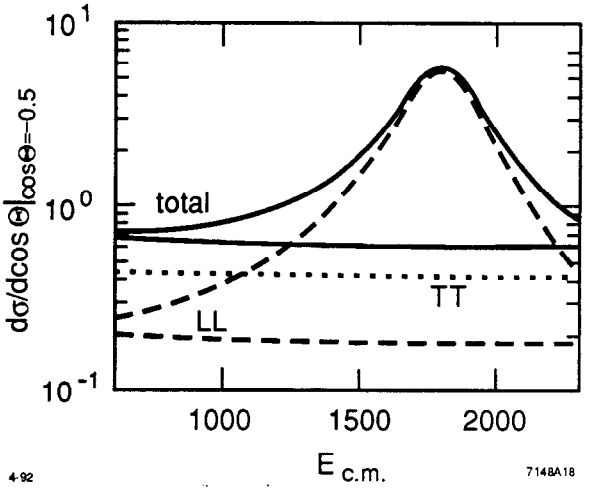

Fig. 11. The effect of a 1.8 TeV techni-ρ resonance in the $W_L^+W_L^- \to W_L^+W_L^-$ channel on the $e^+e^- \to W^+W^-$ cross-section.

is shown in Fig. 11. We incorporate this effect into our analysis by multiplying the standard model amplitude for $e^+e^- \to W_L^+W_L^-$ by the rescattering coefficient F_T defined by

$$F_T \equiv \exp\left[\frac{1}{\pi}\int_0^\infty ds'\delta(s')\left\{\frac{1}{s'-s-i\epsilon}-\frac{1}{s'}\right\}\right]$$

where

$$\delta(s) = \frac{1}{96\pi}\frac{s}{v^2} + \frac{3}{4}\left[\, tanh\left(\frac{M_\rho\Gamma_\rho}{M_\rho^2 - s}\right) + 1\right],$$

$v = 240$ GeV is the Higgs vacuum expectation value, M_ρ is the techni-ρ mass and Γ_ρ is the techni-ρ width. Fig. 12 shows $\mathrm{R_e(F_T)}$ and $\mathrm{I_m(F_T)}$, the real and imaginary parts of F_T for three values of the techni-ρ mass M_ρ. The shortest curve corresponds to $M_\rho = \infty$, the longest curve has $M_\rho = 2\ TeV$, and the intermediate curve has $M_\rho = 3\ TeV$. For each curve the values of $\mathrm{R_e(F_T)}$ and $\mathrm{I_m(F_T)}$ are shown

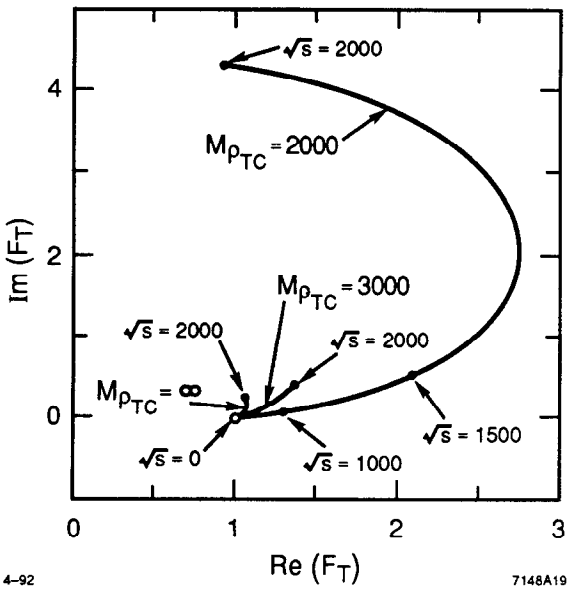

Fig. 12. $I_m(F_T)$ vs. $R_e(F_T)$ for three values of the techni-ρ mass M_ρ.

from $\sqrt{s} = 0$ to $\sqrt{s} = 2$ TeV.

To assess our sensitivity to $R_e(F_T)$ and $I_m(F_T)$ we do another maximum log likelihood analysis. This time we parameterize the log likelihood function with the variables $R_e(F_T), I_m(F_T)$, and $\mathcal{L}$, instead of the variables $\kappa_\gamma, \lambda_\gamma, \kappa_Z, \lambda_Z, \mathcal{L}$. Our log likelihood function $\ln L(R_e(F_T), I_m(F_T), \mathcal{L})$ is otherwise identical to the the one defined in Eq. (6). For the purpose of this discussion we set the coupling parameters $\kappa_\gamma, \lambda_\gamma, \kappa_Z, \lambda_Z$ equal to their standard model values. We have found, however, that this approximation will not be necessary since the variables $\kappa_\gamma, \lambda_\gamma, \kappa_Z, \lambda_Z, R_e(F_T), I_m(F_T)$ were remarkably orthogonal when simultaneous fits of all 6 variables were performed.

The 95% confidence level contours for $R_e(F_T)$ and $I_m(F_T)$ are shown in Fig. 13 for three different e^+e^- center-of-mass energies. At $\sqrt{s} = 1000$ GeV and 1500 GeV we have assumed modest luminosities of 45 fb^{-1} and of 90 fb^{-1}, respectively. We see that at these center-of-mass energies a 1.7 TeV techni-ρ resonance is easily observable. At $\sqrt{s} = 500$ GeV though, and despite the fact that we have assumed a hefty integrated luminosity of of 30 fb^{-1}, the 1.7 TeV techni-ρ is located right on the 95% confidence level contour.

Fig. 14 shows 95% confidence level contours in $R_e(F_T)$, $I_m(F_T)$ space for a larger luminosity at $\sqrt{s} = 1000$ GeV . With 200 fb^{-1} (Fig. 14) it appears possible to detect the presence of a techni-ρ resonance with a mass as large as 4 or 5 TeV.

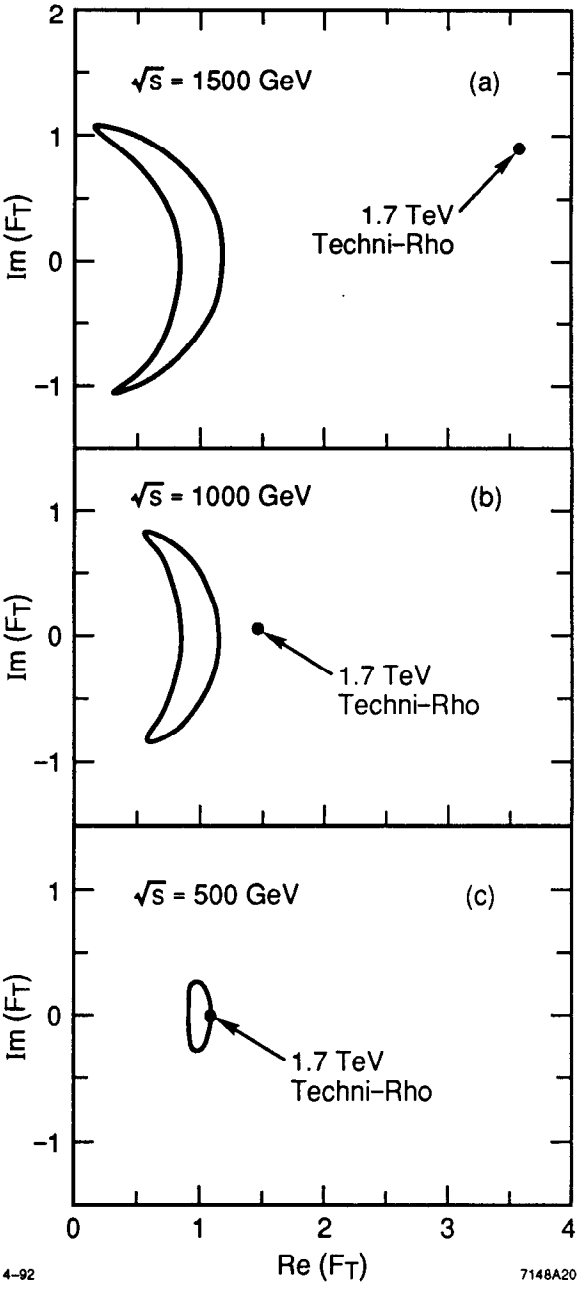

Fig. 13. The 95% confidence level contours for $R_e(F_T)$ and $I_m(F_T)$ for (a) $\sqrt{s} = 1500$, $\mathcal{L} = 90\ fb^{-1}$; (b) $\sqrt{s} = 1000$, $\mathcal{L} = 45\ fb^{-1}$; (c) $\sqrt{s} = 500$, $\mathcal{L} = 30\ fb^{-1}$

3. The Top Quark

The top quark can be studied near threshold or in the continuum. An energy scan across $t\bar{t}$ threshold probes the $t\bar{t}$ potential. The potential is determined mostly by the strong force but can also be affected by Higgs boson exchange[12]. Due to

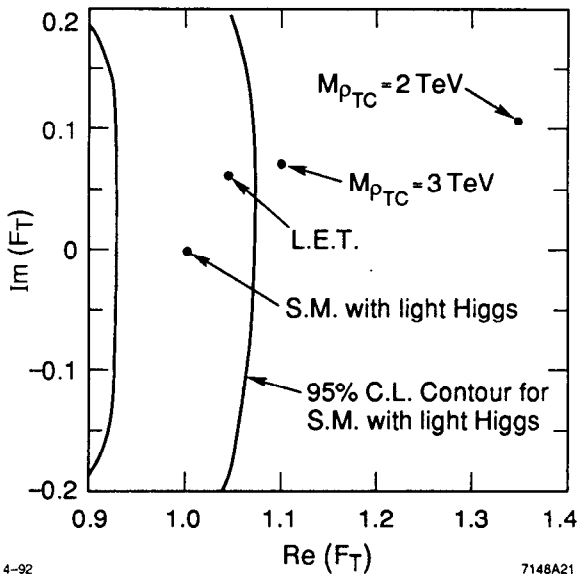

Fig. 14. The 95% confidence level contours for $R_e(F_T)$ and $I_m(F_T)$ for $\sqrt{s} = 1000$, $\mathcal{L} = 200\ fb^{-1}$

the large top mass, perturbative QCD should provide an excellent description of the $t\bar{t}$ potential. The unknown parameters which are measured with an an energy scan across the $t\bar{t}$ threshold region are the top mass M_t, the top decay width Γ_t, the strong coupling constant α_S, and, possibly, the Higgs boson mass M_{ϕ^0} and the top quark Yukawa coupling.

It has been estimated[2] that an energy scan can measure M_t, α_S, and Γ_t with errors of $\Delta M_t = 0.1$ to 0.2 GeV, $\Delta\alpha_S = 0.001$ to 0.005, $\Delta\Gamma_t/\Gamma_t < 0.2$, and that Standard Model Higgs boson exchange can be detected if the Higgs mass is less than 120 GeV or if the top Yukawa coupling is anomalously large.

Additional top physics studies can be made above the $t\bar{t}$ threshold region. An independent measurement of the top mass can be made with an accuracy of $\Delta M_t = 0.2$ GeV using beam energy-momentum constraints on the $t\bar{t}$ final state momenta. Such a measurement can be used, for example, to increase the precision of threshold measurements of α_S and Γ_t. Rare top quark decays can be searched for very effectively by selecting events in which at least one of the top quark decays via $t \rightarrow b\ l^+\ \nu$. Such a selection procedure at an e^+e^- linear collider produces a very high purity $t\bar{t}$ sample. Examples of rare t quark decays are $t \rightarrow s\ W^+$ (thought to be visible if $|V_{ts}|^2 < 0.1$), $t \rightarrow b\ H^+$ where H^+ is a charged Higgs boson, and $t \rightarrow \tilde{\chi}_1^0 \tilde{t}$ where $\tilde{\chi}_1^0$ is the lightest neutralino and $\tilde{t}$ is the stop squark.

A final state helicity analysis of the $t\bar{t}$ final state can be performed to search for structure in the $t\bar{t}\gamma$ and $t\bar{t}\ Z$ production vertices and in the $t\ b\ W^+$ decay

vertex. A study of the $t\ b\ W^+$ vertex would test the expected ratio of longitudinal and transverse W gauge bosons produced in top decay and would be sensitive to a right–handed charged current. The $t\bar{t}$ helicity analysis would be very similar to the W^+W^- helicity analysis described earlier.

4. Higgs Bosons

We denote the standard model Higgs boson by ϕ^0. Large mass standard model Higgs bosons ($M_{\phi^0} > 200$ GeV) will be detected through the WW fusion process $e^+e^- \rightarrow \nu\bar{\nu}\phi^0$. The ϕ^0 decays via $\phi^0 \rightarrow W^+W^-$ or ZZ. Higgs boson with masses as as large as 500 GeV can be detected[13] with 30 fb^{-1} at a $E_{cm} = 1$ TeV.

Intermediate mass Higgs bosons will be detected using the reaction $e^+e^- \rightarrow Z\phi^0$ where the ϕ^0 decays via $\phi^0 \rightarrow b\bar{b}$ and the Z decays via $Z \rightarrow l^+l^-$, $q\bar{q}$, or $\nu\bar{\nu}$. This is how LEP searches for the standard model Higgs boson and the same methods work at NLC.

Of greater interest is how the NLC can be used to measure the branching ratios of various Higgs decay modes. For example, the branching ratios for $\phi^0 \rightarrow b\bar{b}$, $\phi^0 \rightarrow WW^*$, $\phi^0 \rightarrow \tau^+\tau^-$, and $\phi^0 \rightarrow c\bar{c} + gg$ can be be measured[14] with the errors shown in Fig. 15. The error bars are superimposed on a plot of the branching ratios of the lightest Higgs boson h^0 of the minimal supersymmetric extension to the standard model (MSSM). The branching ratios of the h^0 are plotted as a function of $\tan\beta$, the ratio of the vacuum expectation values of the two Higgs doublets of the MSSM. The branching ratios of the h^0 with small $\tan\beta$ coincide with the branching ratios of the standard model Higgs boson ϕ^0.

The $\gamma\gamma$ partial width of a Higgs boson is of special interest because it receives contributions from all electrically charged elementary particles which couple to the particular Higgs boson[15]. An elementary particle's contribution to the $\gamma\gamma$ partial width of the ϕ^0, for example, approaches a nonzero asymptotic value as the mass of the elementary particle approaches infinity. A measurement of the $\gamma\gamma$ partial width of the ϕ^0 can therefore probe physics at very large energy scales.

By colliding two beams of laser light which have been backscattered off the e^- and e^+ beams of an e^+e^- linear collider[16], the partial width $\Gamma(\phi^0 \rightarrow \gamma\gamma)$ can be measured. See Ref. 17 for a discussion of this measurement.

5. Supersymmetry

Future e^+e^- linear colliders will be in a position to study all of the supersymmetric partners of the γ, Z, and W, and of the three generations of fermions. They

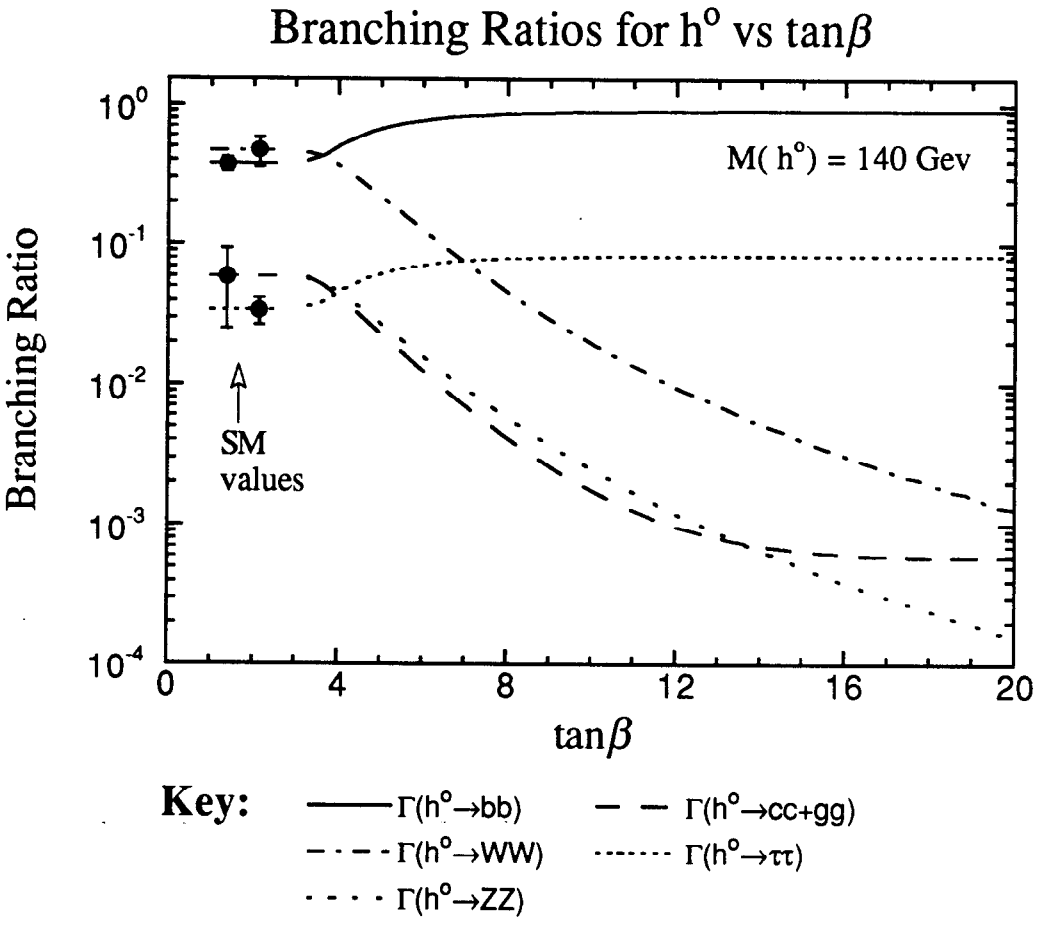

Fig. 15. Higgs branching ratio measurement errors.

will also be able to study in detail the Higgs bosons of supersymmetric theories.

We list the the additional particles required[18,19] by the MSSM:

1. Two neutral scalar Higgs particles, h^0 and H^0, a neutral pseudoscalar Higgs particle A^0, and a charged Higgs particle H^+.
2. One scalar neutrino $\tilde{\nu}_l$ for each of the three ordinary neutrinos and a left and right-handed sfermion $\tilde{f}_L$ and $\tilde{f}_R$ for each massive fermion.
3. Four neutralinos $\tilde{\chi}_1^0$, $\tilde{\chi}_2^0$, $\tilde{\chi}_3^0$, and $\tilde{\chi}_4^0$. Each neutralino is a mixture of the SUSY partners of the photon, the Z^0 and the neutral components of the Higgs doublets.
4. Two charginos $\tilde{\chi}_1^+$ and $\tilde{\chi}_2^+$. Each chargino is a mixture of the fermion partners of the $W^\pm$ and the charged components of the Higgs doublets.

5. The gluino $\tilde{g}$, which is the fermion partner of the gluon.

The Higgs mass spectrum of the MSSM is determined by two parameters which can be taken to be $\tan\beta$ and the mass M_{A^0} of the pseudoscalar Higgs. The entire parameter space of $\tan\beta$ versus M_{A^0} can be easily covered at an e^+e^- linear colliers with 10 fb^{-1} at $E_{cm} = 500$ GeV by searching for $e^+e^- \rightarrow h^0Z$ and $e^+e^- \rightarrow H^0Z$. In fact, less luminosity and less center–of–mass energy is required to cover the entire parameter space[20].

An e^+e^- linear collider can be used to study the spectrum of Higgs bosons in supersymmetric theories. An excellent example is given by Janot[21]. who studied the process $e^+e^- \rightarrow \gamma\, X\, Y$ where $X \rightarrow \tau^+\tau^-$, $Y \rightarrow q\bar{q}$, $X,Y = h^0$, H^0, A^0, Z, and γ is a beamstrahlung or initial state bremsstrahlung photon. Beam energy-momentum contraints are used to solve for E_γ, $E_{\tau+}$, $E_{\tau-}$, and E_Y, the energies of four of the final state particles. The momentum of the τ^+ and τ^- are determined by $E_{\tau+}$, $E_{\tau-}$, the measured directions of the $\tau^\pm$ decay products, and the τ mass. The momentum of the Y particle is determined by E_Y and the measured velocity of the system composed of the visible decay products of the Y. After imposing cuts to suppress background, the masses of the X and Y particles are plotted in the same histogram. A mass peak is seen at the Z mass from the process $e^+e^- \rightarrow ZZ$, but, in addition, mass peaks from the h^0, H^0 and A^0 appear from the processes $e^+e^- \rightarrow h^0Z$, $e^+e^- \rightarrow H^0Z$, $e^+e^- \rightarrow h^0A^0$, and $e^+e^- \rightarrow H^0A^0$.

If supersymmetric particles exist then e^+e^- linear colliders will be excellent facilities at which to study them. SUSY phenomenology will be very complicated. In general there will be $\tilde{f}_L$–$\tilde{f}_R$ mixing, intergenerational mixing, cascade decays of heavier SUSY particles such as squarks and the heavier neutralinos, and new sources of CP violation. e^+e^- linear colliders possess powerful tools with which to disentangle such a complex spectrum of states. Among the tools are initial state polarization of the e^- beam, high analyzing power of final state polarization, full reconstruction of final states with multiple numbers of leptons, quark jets, W's and Z's, and beam constrained fits of the momenta of heavy particles.

As an example we consider the process $e^+e^- \rightarrow \tilde{\chi}_1^+\tilde{\chi}_1^-$ where $\tilde{\chi}_1^+$ is the lightest chargino. There are three tree–level graphs contributing to the process $e^+e^- \rightarrow \tilde{\chi}_1^+\tilde{\chi}_1^-$: the γ s–channel annihilation, the Z s–channel annihilation, and the $\tilde{\nu}_e$ t–channel exchange graphs. The coupling of the $\tilde{\chi}_1^+$ to the photon is just given by its charge. The left and right–handed couplings of the $\tilde{\chi}_1^+$ to the Z, which we denote by O_L and O_R respectively, will be different and will depend on the relative amounts of wino and charged Higgsino in the $\tilde{\chi}_1^+$. The coupling at the e^- $\tilde{\chi}_1^+$ $\tilde{\nu}_e$ vertex will depend on the polarization of the inital state e^-, the SU(2) gauge coupling constant g, and the relative amounts of wino and charged Higgsino in the $\tilde{\chi}_1^+$. The coefficient at the e^- $\tilde{\chi}_1^+$ $\tilde{\nu}_e$ vertex which depends on the relative amounts of wino and charged Higgsino in the $\tilde{\chi}_1^+$ is denoted by V.

In the MSSM the coupling coefficients $O_{\rm L}$, $O_{\rm R}$, and V depend on the W^3–ino Majorana mass parameter M_2, the Higgs superpotential parameter μ and $\tan\beta$: $O_{\rm L} = O_{\rm L}(M_2, \mu, \tan\beta)$ $O_{\rm R} = O_{\rm R}(M_2, \mu, \tan\beta)$, and $V = V(M_2, \mu, \tan\beta)$. The cross–section for $e^+e^- \rightarrow \tilde{\chi}_1^+\tilde{\chi}_1^-$ will depend on the initial state e^- polarization, $O_{\rm L}$, $O_{\rm R}$, and $V^2/M^2_{\tilde{\nu}_e}$, where $M_{\tilde{\nu}_e}$ is the mass of the $\tilde{\nu}_e$. We assume that the $\tilde{\chi}_1^+$ decays 100% via $\tilde{\chi}_1^+ \rightarrow W^+\tilde{\chi}_1^0$ where $\tilde{\chi}_1^0$ is the lightest neutralino and the lightest supersymmetric particle. This will be the case, for example, if the only SUSY particles lighter than the $\tilde{\chi}_1^+$ are the $\tilde{\chi}_1^0$ and the the right handed selectron $\tilde{e}_{\rm R}$ — a not unreasonable assumption.

We denote the masses of the $\tilde{\chi}_1^+$ and the $\tilde{\chi}_1^0$ by $M_{\tilde{\chi}_1^+}$ and $M_{\tilde{\chi}_1^0}$ respectively. Within the MSSM, we have $M_{\tilde{\chi}_1^+}$=$M_{\tilde{\chi}_1^+}(M_2, \mu, \tan\beta)$ and $M^0_{\tilde{\chi}_1}$=$M^0_{\tilde{\chi}_1}(M_1, M_2, \mu, \tan\beta)$, where M_1 is the Bino Majorana mass parameter. The energy and angle distributions of the W^+ and W^- bosons in the process $e^+e^- \rightarrow \tilde{\chi}_1^+\tilde{\chi}_2^- \rightarrow W^+W^-\tilde{\chi}_1^0\tilde{\chi}_1^0$ will depend on the inital state e^- polarization, $V^2/M^2_{\tilde{\nu}_e}$, $O_{\rm L}$, $O_{\rm R}$, $M_{\tilde{\chi}_1^+}$ and $M^0_{\tilde{\chi}_1}$. By collecting data half the time with right-handed longitudinally polarized electrons in the initial state, and half the time with left-handed electrons, and by binning the energy and polar angle of the $W^\pm$, the maximum likelihood method can be used to fit for $V^2/M^2_{\tilde{\nu}_e}$, $O_{\rm L}$, $O_{\rm R}$, $M_{\tilde{\chi}_1^+}$ and $M^0_{\tilde{\chi}_1}$.

If we assume that $\tan\beta$ has been measured using the measured Higgs boson mass M_{h^0} and the branching ratio for $h^0 \rightarrow WW^*$, then from the measured values of $O_{\rm L}$, $O_{\rm R}$, and $M_{\tilde{\chi}_1^+}$ we can extract M_2 and μ, and perform a MSSM consistency check since we are solving for two parameters using three measurements. Our measured value of $M^0_{\tilde{\chi}_1}$ will give us an estimate of M_1 and we can check the consistency of the Grand Unified Theory (GUT) relation between M_1 and M_2. Our measured values of M_1 and M_2 can be used to predict the mass of the gluino.

With our measured values M_2, μ and $\tan\beta$ we can solve for the parameter V. We can then use our fitted value of $V^2/M^2_{\tilde{\nu}_e}$ to estimate $M_{\tilde{\nu}_e}$ or to put a lower limit on $M_{\tilde{\nu}_e}$. For more discussion on this topic and quantitative examples see Ref. 2.

Acknowledgments

I would like to thank the organizers of this conference for an enjoyable stay at the I.C.T.P. This work was supported in part by U.S. Department of Energy contract DE-AC03-76SF00515.

REFERENCES

1. R. Ruth, in *Proc. of Workshop on Physics and Experiments with Linear Colliders*, Saariselka, Finland (1991) and SLAC-PUB-5729 (1992).
2. JLC Group, S. Matsumoto *et al.*, KEK Report 92-16 (1992)
3. K. Balewski *et al.*, preprint DESY-91-153 (1991)
4. H. Padamsee, in *Proc. of 1991 IEEE Particle Accelerator Conf.*, San Francisco, Ca. (1991) and preprint CLNS-91-1080 (1991).
5. D. Burke, in *Proc. of Workshop on Physics and Experiments with Linear Colliders*, Saariselka, Finland (1991) and SLAC-PUB-5791 (1992).
6. T. Barklow, P. Chen, and W. Kozanecki, in *Proc. of ECFA Workshop on Physics with Linar Colliders*, Hamburg, Germany (1991) and SLAC-PUB-5718 (1992).
7. K. Hagiwara, R.D. Peccei, D. Zeppenfeld, and K. Hikasa, *Nucl. Phys.* **B282,** 253 (1987).
8. G.L. Kane, J. Vidal, and C.-P. Yuan, *Phys. Rev.* **D39**, 2617 (1989).
9. A.de Rujula,M.B.Gavela,P. Hernandez, and E.Masso, preprint CERN-TH.6272/91 (1991); K.Hagiwara,S.Ishihara,R.Szalapski, D.Zeppenfeld, preprint MAD/PH/690 (1992).
10. M.E.Peskin, in *Physics in Collision 4*, A.Seiden, ed. (Editions Frontieres, Gif-sur-Yvette, 1984).
11. K.Hikasa, plenary talk at this workshop and preprint KEK-TH-319 (1992)
12. M. Strassler and M. Peskin, *Phys. Rev.* **D43**, 1500 (1991).
13. P. Burchat, D. Burke, and A. Petersen, *Phys. Rev.* **D38**, 2735 (1991).
14. M. Hildreth, SLAC-PUB-6036 (1993).
15. J. Gunion and H. Haber in *Proc. of 1990 DPF Summer Study on High Energy Physics*, Snowmass, Colorado (1990) and preprint SCIPP-90-22 (1990).
16. I.F. Ginzburg *et al.*, *Nucl. Instrum. Methods* **205**, 47 (1983); I.F. Ginzburg *et al.*, *Nucl. Instrum. Methods* **219**, 5 (1984); V.I. Telnov, *Nucl. Instrum. Methods* **A294**, 72 (1990);
17. T. Barklow in *Proc. of 1990 DPF Summer Study on High Energy Physics*, Snowmass, Colorado (1990) and SLAC-PUB-5364 (1990).
18. H. Haber and G. Kane *Phys. Rept.* **117,** 75 (1985).
19. J. Gunion and H. Haber *Nucl. Phys.* **B272,** 1 (1986).
20. P. Janot, preprint LAL 92-07 (1992).
21. P. Janot, preprint LAL 91-61 (1991).